Theory and applications of ray chaos to underwater acoustics

I. P. Smirnov*
Nizhny Novgorod State University, 23 Gagarina Prospekt, 603600 Nizhny Novgorod, Russia

A. L. Virovlyansky†
Institute of Applied Physics, Russian Academy of Science, 46 Ul'yanov Street, 603600 Nizhny Novgorod, Russia

G. M. Zaslavsky‡
Courant Institute of Mathematical Sciences, New York University, 251 Mercer Street, New York, New York 10012
and Department of Physics, New York University, 2-4 Washington Place, New York, New York 10003
(Received 19 December 2000; published 29 August 2001)

Chaotic ray dynamics in deep sea propagation models is considered using the approaches developed in the theory of dynamical chaos. It has been demonstrated that the mechanism of emergence of ray chaos due to overlapping of nonlinear ray-medium resonances should play an important role in long range sound propagation. Analytical estimations, supported by numerical simulations, show that for realistic values of spatial periods and sound speed fluctuation amplitudes associated with internal-wave-induced perturbations, the resonance overlapping causes stochastic instability of ray paths. The influence of the form of the smooth unperturbed sound speed profile on ray sensitivity to the perturbation is studied. Stability analysis has been conducted by constructing the Poincaré maps and examining depth differences of ray trajectories with close take-off angles. The properties of ray travel times, including fractal properties of the time front fine structures, under condition of ray chaos have been investigated. It has been shown that the coexistence of chaotic and regular rays, typical for dynamical chaos, leads to the appearance of gaps in ray travel time distributions, which are absent in unperturbed waveguides. This phenomenon has a prototype in theory of dynamical chaos called the stochastic particle acceleration. It has been shown that mesoscale inhomogeneities with greater spatial scales than that of internal waves, create irregular local waveguide channels in the vicinity of the axis (i.e., sound speed minimum) of the unperturbed waveguide. Near-axial rays propagating at small grazing angles, ''jump'' irregularly between these microchannels. This mechanism determines chaotic behavior of the near-axial rays.

DOI: 10.1103/PhysRevE.64.036221 PACS number(s): 05.45.Ac

I. INTRODUCTION

In the past decade it has been realized that the phenomenon of ray chaos plays a significant role in long range sound propagation in deep sea [1–9]. Numerical simulations have demonstrated that under typical conditions of deep sea ray trajectories are highly unstable and exhibit extreme sensitivity to starting parameters. Initially close rays diverge exponentially with range and numerical estimations of inverse Lyapunov exponents—main quantitative characteristics of this divergence—are usually of order of a few hundreds kilometers [6–8]. On the other hand, solving of underwater acoustics inverse problems aimed at monitoring of large scale features of the ocean temperature field, implies carrying out acoustic measurements at acoustic paths of thousands kilometer long [10–13]. It is quite clear that at so long ranges chaotic properties of the ray structure can not be ignored.

The chaotic ray motion in underwater acoustic waveguides is analogous to chaotic dynamics of nonintegrable Hamiltonian systems in classical mechanics. The main goal of this paper is to demonstrate that the methods developed in the theory of dynamical chaos, being applied to problems of long range sound propagation in the ocean, give insight into basic mechanisms determining ray structure range variations. We discuss how phenomena known in the theory of dynamical chaos, can manifest themselves in underwater acoustics.

In many studies on ray chaos in acoustic waveguides, attention is confined to environmental models with periodic range dependence [1–5]. The reason is partly that properties of chaotic ray dynamics in such waveguides are identical (at least, formally) to extensively studied properties of chaotic dynamics of a nonlinear oscillator driven by an external periodic force [1,2]. Further, periodic models are not so artificial as they may look at first glance: a rather realistic environment can be synthesized out of comparatively small number of periodic terms. For example, in Ref. [8] it has been demonstrated that predictions made in the scope of a ten-terms model can be in reasonable agreement with experimental data.

The objective of the present paper is to show how some known properties of Hamiltonian chaotic dynamics reveal themselves in periodic environmental models of underwater acoustics. We focus here on two issues. One of them is a role of the ray-medium resonance phenomenon as an important factor of stochastic ray instability. We consider a model with a smooth range-independent background sound-speed profile

*Electronic address: ivansm@mail.ru
†Electronic address: viro@hydro.appl.sci-nnov.ru
‡Electronic address: zaslav@cims.nyu.edu

and weak inhomogeneities induced by two periodic internal-wave modes. With this example we discuss the role of ray-medium resonances in the emergence of ray chaos. Analytical estimations supported by numerical simulation show that for realistic values of spatial periods and sound-speed fluctuation amplitudes associated with this perturbation, overlapping of resonances is possible. According to the Chirikov's heuristic criterion, this overlapping gives rise to strong ray chaos [14–16]. It is clear that the overlapping condition depends on the parameters of both, unperturbed profile and perturbation. We argue that studying of ray-medium resonances gives insight into strong dependence of global ray sensitivity on a background sound-speed profile demonstrated in Ref. [8].

Much of the present paper is concerned with investigating of ray travel times. This is the second important issue addressed here. So far, the ray travel time has been the main signal parameter in the underwater acoustics experiments from which inversions have been performed to reconstruct ocean temperature field [10,11]. That is why chaotic properties of this signal characteristic are of considerable interest. On the other hand, from the viewpoint of opticomechanical analogy, the ray travel time is an analog to mechanical action, i.e., of such a characteristic of dynamical systems that is, typically, not measured experimentally and for this reason has not received much attention in studies on dynamical chaos. Using numerical simulation we study how chaotic behavior of ray trajectories manifests itself in the travel time dependence on the starting momentum and in the so-called time front representing ray arrivals in depth-time plane.

The most part of this paper is devoted to studying of environmental models describing the influence of internal waves on sound transmission. The point is that the internal waves are considered as a main factor responsible for emergence of ray chaos at long range wave propagation. At the end of the paper we shortly discuss the role of the so-called mesoscale inhomogeneities whose spatial and temporal scales are considerably greater than that of internal waves. We argue that the mesoscale inhomogeneities cause chaotic behavior of near-axial rays and the mechanism determining this chaotic dynamics has some specific features that differentiate it from the mechanisms defining ray chaos due to internal waves.

In studying ray dynamics we shall neglect the horizontal refraction. This assumption is widely used in underwater acoustics because the cross-range gradients of the sound speed are typically two orders of magnitude smaller than the vertical gradients. That is why the sound propagation is well described as two dimensional (having no out-of-plane scattering) [8,17].

The paper is organized as follows. In Sec. II we give a brief description of the nonlinear ray-medium resonance and discuss the role of resonance overlapping in the emergence of ray chaos. The perturbation theory of resonances, including Chirikov's heuristic criterion of chaos emergence due to the resonance overlapping, is presented in Sec. II A. This theory is formulated using the Hamiltonian formalism in terms of the action-angle canonical variables. In Sec. II B the general relations are applied to study stochastic ray instability and its dependence on parameters of the perturbation and that of the smooth background profile. This is done using ray simulation in an underwater acoustic waveguide with range-dependent perturbations due to two internal-wave modes. Stability analysis is conducted by constructing the Poincaré maps and examining depth differences of ray trajectories with close take-off angles. It is investigated numerically how the phenomenon of resonance overlapping affects ray dynamics in realistic environmental models considered in this section.

The emphasis in Sec. III is on properties of ray travel times under conditions of ray chaos. We study how the coexistence of regular and chaotic rays manifests itself in the structure of ray arrivals. The phenomenon of stickiness destroying the uniformity of the motion of chaotic rays, and the concept of ''chaotic wave transmission'' introduced in Ref. [18] are shortly discussed. By numerical simulation we show that the presence of a sharp boundary between regions of phase plane occupied by these two types of rays, lead to appearance of the gap in the distribution of ray travel times. In this section we also investigate diffusion of the action and fractal properties of travel times of chaotic rays.

In Sec. IV we show that the phenomenon of chaotic particle acceleration known in the theory of dynamical chaos [15], has an analog in ray dynamics. The presence of the gap in the ray travel time distribution is interpreted from the viewpoint of this mechanism. In this section we discuss how chaotic ray motion reveals itself in different features of the time front.

In Sec. V we examine the ray structure in the presence of mesoscale perturbations. Here we use an environmental model constructed on the basis of real hydrographic data. It is demonstrated numerically that mesoscale inhomogeneities give rise to chaotic motion of near-axial rays and the basic mechanism determining the stochastic instability of these rays is identified.

In Sec. VI the results of this work are summarized.

II. RAY-MEDIUM NONLINEAR RESONANCE

A. Perturbation theory for the resonances

In this section the Hamiltonian formalism used for ray dynamics analysis is briefly discussed and short description of ray-medium resonance phenomenon in terms of action-angle canonical variables is provided using this, actually known, formalism [1,2]. As it has been indicated already, the smallness of cross-range gradients of the sound speed allows one to neglect the horizontal refraction and describe the sound propagation as two dimensional.

1. Basic equations for ray dynamics

Consider a two-dimensional underwater acoustic waveguide with the sound speed c being the function of depth z and range r. The z axis is directed downward. The ray trajectory obeys the Hamilton equations

$$\frac{dz}{dr}=\frac{\partial H}{\partial p}, \quad \frac{dp}{dr}=-\frac{\partial H}{\partial z}, \tag{1}$$

with the Hamiltonian

$$H=-\sqrt{n^2(r,z)-p^2}. \tag{2}$$

Here $n(r,z)=c_0/c(r,z)$ is the refractive index, c_0 is some reference sound-speed value, and the variable p presents an analog to the mechanical momentum. The Hamiltonian H and momentum p are connected to the current ray grazing angle α by

$$H=-n\cos\alpha, \quad p=n\sin\alpha. \tag{3}$$

The ray travel time t is an analog to mechanical action and is given by the integral

$$t=\frac{1}{c_0}\int (pdz-Hdr). \tag{4}$$

In many problems of underwater acoustics the sound speed field $c(r,z)$ can be modeled as a superposition of a smooth range-independent background sound-speed profile $\overline{c}(z)$ and a weak range-dependent perturbation $\delta c(r,z)$:

$$c(r,z)=\overline{c}(z)+\delta c(r,z). \tag{5}$$

In environmental models used in underwater acoustics [17] the condition

$$|\delta c|\ll\Delta c\ll c_0 \tag{6}$$

is typically met, where Δc is the maximum variation of $\overline{c}$, and the constant c_0 is chosen to be the minimum value of $\overline{c}(z)$. Then the Hamiltonian can be approximately rewritten in the form

$$H=\overline{H}+V, \tag{7}$$

where

$$\overline{H}=-\sqrt{\overline{n}^2-p^2}, \quad \overline{n}(z)=\frac{c_0}{\overline{c}(z)},$$

$$V(r,z)=\frac{\delta c(r,z)}{c_0}. \tag{8}$$

In real deep ocean acoustic waveguides only those rays that propagate at grazing angles smaller than $10°-15°$ survive at long ranges (steeper rays interact with a lossy bottom). We shall consider here only such rays. Their momenta satisfy the condition

$$p\ll|H|\sim 1. \tag{9}$$

In the range-independent waveguide ($V=0$) with the Hamiltonian $\overline{H}$, the conservation law $\overline{H}=E$ holds true along the ray trajectory with the constant E being an analog to the mechanical energy. The explicit expression for the momentum p as a function of E and z is $p(E,z)=\pm\sqrt{\overline{n}^2(z)-E^2}$. All the trajectories for $V=0$ are periodic curves. The coordinates of their upper and lower turning points ($z_{\max}$ and $z_{\min}$, respectively) are functions of the "energy," E, and determined by the equation $\overline{n}(z)=-E$.

An important characteristics of ray trajectories that is widely used in both classical mechanics and ray theory, is the so-called action variable I related to E by [19]

$$I=\frac{1}{2\pi}\oint dz\, p(E,z)=\frac{1}{\pi}\int_{z_{\min}}^{z_{\max}} dz\sqrt{\overline{n}^2-E^2}, \tag{10}$$

where the integration goes over the period of the ray trajectory. Equation (10) defines the function $E(I)$. Now the turning point coordinates, $z_{\min}$ and $z_{\max}$, can also be regarded as functions of I.

The canonical transformation from (p,z) variables to the action-angle variables (I,θ) is given by the pair of equations [19]

$$p=\frac{\partial G(z,I)}{\partial z}, \quad \theta=\frac{\partial G(z,I)}{\partial I}, \tag{11}$$

with the generating function

$$G(z,I)=\int_{z_{\min}}^{z} dz\sqrt{\overline{n}^2(z)-E^2}. \tag{12}$$

Note, that p and z are periodic functions of the angle variable θ, i.e., $p(I,\theta)=p(I,\theta+2\pi)$, $z(I,\theta)=z(I,\theta+2\pi)$.

2. Resonances

In the range-dependent environment ($V\neq 0$) we define the action-angle variables using the same relations [given in Eqs. (11) and (12)] as in the unperturbed waveguide. The Hamiltonian equations in the new variables take the form [1]

$$\frac{dI}{dr}=-\frac{\partial V}{\partial\theta}, \quad \frac{d\theta}{dr}=\omega(I)+\frac{\partial V}{\partial I}, \tag{13}$$

where

$$\omega(I)=d\overline{H}(I)/dI \tag{14}$$

is the spatial frequency of the trajectory oscillations in the unperturbed waveguide.

Now let us turn our attention to an environmental model with periodic range dependence. In this case the perturbation $V(r,z(I,\theta))$ is periodic in r and θ and it can be represented in the form of the Fourier series

$$V=\frac{1}{2}\sum_{m,q} V_{m,q}(I)e^{i(m\theta-q\Omega_0 r)}+\text{c.c.}, \tag{15}$$

where the symbol c.c. denotes complex conjugation.

A group of ray trajectories are captured in a ray-medium resonance if their action variables are close to I_0 satisfying the condition

$$m\,\omega(I_0)=q\Omega_0, \tag{16}$$

with m and q being two integers. The ray trajectory trapped into the resonance can be analytically described using a

simple perturbation theory (see, for example, Refs. [1,2]). Here we shall use only one result of this analysis, namely, an estimation of the resonance width.

It can be shown that action variables of the trapped rays belong to the interval $I_0-\Delta I_{\max}<I<I_0+\Delta I_{\max}$, where

$$\Delta I_{\max}=2\sqrt{V_0/|\omega'|} \tag{17}$$

with V_0 being the amplitude of the resonant term in sum (15). Equation (17) defines a half-width of the resonance in terms of action. Each trapped ray oscillates with some spatial frequency. The width of the resonance in terms of spatial frequency can be approximately estimated as

$$\Delta\omega=|\omega'|\Delta I_{\max}=2\sqrt{V_0|\omega'|}. \tag{18}$$

Estimations (17) and (18) are made for each individual resonance ignoring all the other resonances. That is why they have a good sense only when perturbation is small enough, i.e.,

$$\varepsilon=\frac{V_0}{|H(I_0)-H(0)|}\ll 1. \tag{19}$$

In the denominator we subtract the constituent of the Hamiltonian independent of I, which may be arbitrary large or small depending on a choice of the reference sound speed c_0. The applicability conditions of this approach are discussed in Refs. [1,2]. Here we will only note that the main condition is

$$\varepsilon\ll\alpha\ll\frac{1}{\varepsilon}, \tag{20}$$

where

$$\alpha=\left|\frac{d\omega(I_0)}{dI}\right|\frac{I_0}{\omega(I_0)} \tag{21}$$

is a parameter characterizing the degree of nonlinearity.

3. Degree of nonlinearity in a typical model of underwater acoustic waveguide

Consider the so-called canonical sound-speed profile, or the Munk profile, widely used in underwater acoustics to model wave transmission through a deep ocean [17]:

$$\overline{c}(z)=c_0[1+\varepsilon(e^{-\eta}+\eta-1)],$$

$$\eta=2(z-z_a)/B, \tag{22}$$

where $c_0=1.49$ km/s, $z_a=1$ km is the sound-speed axis (depth corresponding to the minimum of sound speed), $\varepsilon=0.0057$, and $B=1$ km. This profile is shown by a dashed line in the left panel of Fig. 1 (other curves presented in this figure will be discussed later). In what follows this profile will be used in our numerical simulations. Now, with this example, we want to demonstrate dependencies of ω and $d\omega/dI$ on the action variable which are typical for ocean-acoustic propagation models.

In Figs. 2(a) and 2(b) this is done for a waveguide with

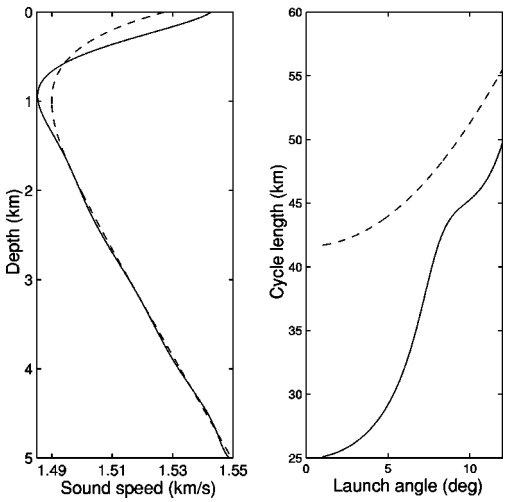

FIG. 1. Sound-speed profiles (left panel) and cycle lengths against launch angles for rays starting from the waveguide axis (right panel). Dashed line – profile 1, solid line – profile 2.

sound-speed profile (22) under assumption that the bottom is located at 6 km depth. Note, that the interval of actions, I, from 0 to about 0.2 km corresponds to ray trajectories that do not strike the surface or the bottom (the bottom is located at 6 km depth). The interval from 0.2 to 0.43 km correspond to surface-bounce rays, but these ray do not strike the bottom. Larger values of I correspond to rays reflecting off both surface and bottom. These three intervals are echoed in ω dependence on I presented in Fig. 2(a) and they are much more apparent in Fig. 2(b) where the dependence of $d\omega/dI$ on I is shown.

Let us stress that for purely refracted rays, propagating without interaction with both surface and bottom, the angular frequency ω decreases with I. This property is typical of

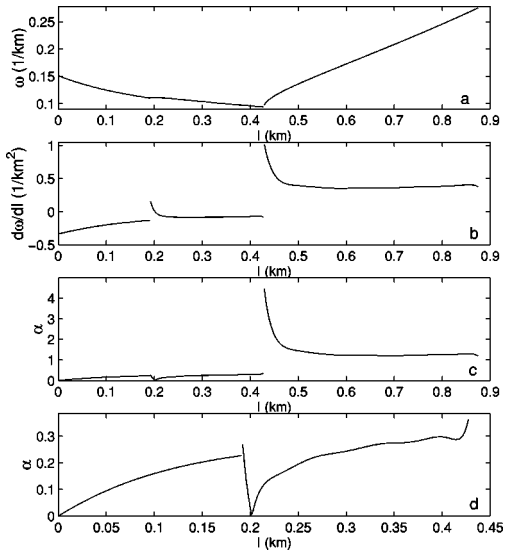

FIG. 2. Angular frequency ω of ray oscillations (a) and its derivative with respect to the action variable I (b) as functions of I. The nonlinearity parameter α against I (c) and a closer view of this dependence for rays propagating without reflection off the bottom (d).

sound-speed profiles in deep sea. It can also be formulated in a slightly other form: the cycle length in underwater acoustic waveguide usually increases with the grazing angle at which the ray crosses the sound-speed axis (see the dashed line in the left panel of Fig. 1).

Figures 2(c) and 2(d) show the parameter α, degree of nonlinearity defined in Eq. (21), as a function of the action I. Figure 2(c) shows this parameter for all three types of rays considered above. Figure 2(d) presents a portion of the above curve corresponding to rays propagating without reflection off the bottom.

4. Overlapping of resonances

If there exist several resonances centered at different spatial frequencies (at different values of I_0) properties of ray motion considerably depend on whether these resonances overlap or not. Chaotic rays exist in any case. But in the case of isolated resonances they typically form the so-called stochastic layers in the neighborhood of separatrices dividing the areas in the phase space occupied by trapped and untrapped rays [2]. The action variables of rays belonging to such layers are close to $I_0 \pm \Delta I_{\max}$, i.e., to borders of the interval determined by Eq. (17). Since the stochastic layers usually occupy only a small fraction of the phase space this situation is called the weak chaos.

Overlapping of resonances gives rise to much more pronounced chaotic ray motion. Consider two resonances centered at actions I_1 and I_2. The corresponding spatial frequencies are $\omega_1 = \omega(I_1)$ and $\omega_2 = \omega(I_2)$. The widths of these resonances in terms of action (spatial frequency), estimated by applying Eq. (17) [Eq. (18)], we denote by ΔI_1 and ΔI_2 ($\Delta\omega_1$ and $\Delta\omega_2$). If the total width of both resonances $\Delta I = (\Delta I_1 + \Delta I_2)$ is less than the difference between the centers of the resonances $\delta I = |I_2 - I_1|$, then the resonances are isolated. Otherwise, the resonances overlap that leads to their interaction giving rise to chaotic motion. According to the heuristic Chirikov's criterion, the system exhibits strong chaos if the condition

$$\frac{\Delta I}{\delta I} > Q \tag{23}$$

is met [14–16]. Here Q is a constant close to unity. In terms of spatial frequencies, this criterion takes the form

$$\frac{\Delta\omega}{\delta\omega} > Q, \tag{24}$$

where $\delta\omega = |\omega_2 - \omega_1|$ and $\Delta\omega = (\Delta\omega_1 + \Delta\omega_2)$.

The overlap of resonances begins when their separatrices touch each other. Neglecting the deformation of the separatrix due to the presence of the neighboring resonance yields the simplest form of the Chirikov's criterion with $Q = 1$. This gives an order-of-magnitude estimate of a perturbation strength at which rays begin to exhibit the strong chaotic motion. In order to obtain a more accurate result one should take into account a finite width of the stochastic layer surrounding the separatrix as well as the influence of high-order resonances that are not explicitly present in the Hamiltonian $\overline{H}(I) + V(I, \theta, r)$ with V defined by Eq. (15), and which arise in higher-order approximations of the perturbation theory. A detailed analysis of these factors (see Refs. [14,16]) leads to more precise estimates of the constant Q. In particular, for the so-called standard map it has been found that $Q \simeq 2/\pi \simeq 0.64$. It is believed that the value $Q = 2/\pi$ is rather universal although there is no rigorous proof of that.

Let us emphasize an important point. Chirikov's criteria (23) and (24) not only indicate the fact of the emergence of strong chaos. They also give simple, albeit rough, quantitative estimations characterizing a region of phase plane occupied by chaotic rays. The quantities ΔI and $\Delta\omega$ provide estimations of intervals of actions and spatial frequencies, respectively, corresponding to chaotic ray paths.

B. Ray chaos simulation

There exists a ''regular'' way to describe or identify chaotic dynamics using phase space portrait, Poincaré map, Lyapunov exponent, etc. Although all of them can not be used in a straightforward way for the underwater acoustics diagnostics. The reason is evident since one cannot track rays at ranges of thousands kilometers. Temporal evolution of the arriving wave fronts and intensities of signals at different depths at some fixed ranges are the main diagnostic entities used in the contemporary experiments. In this section we start to study how chaotic motion reveals itself in ray structure characteristics at a given range.

1. Environmental models

In this section effects related to resonance overlapping will be investigated numerically using idealized models of underwater long-range sound propagation.

Two background sound-speed profiles $\overline{c}(z)$ shown in the left panel of Fig. 1 and hereafter referred to as profile 1 and profile 2, will be considered. As it has been indicated already, profile 1 is the so-called canonical Munk profile defined in Eq. (22). Although both profiles look similar, rays propagating in the corresponding waveguides without surface and bottom interactions have significantly different intervals of cycle lengths as it is seen in the right panel of Fig. 1. With this example we shall demonstrate that this difference can result in different stochastic instabilities of ray trajectories with respect to a weak range-dependent perturbation.

We consider a sound-speed perturbation in the form

$$\delta c(r,z) = e^{-3z/2B} \sum_{j=1}^{J} A_j \sin(j\pi e^{-z/B}) \cos(k_j r + \lambda_j), \tag{25}$$

where each term on the right accounts for a contribution from an internal-wave mode with the horizontal wave number k_j, A_j, and λ_j are random amplitudes and phases, respectively, B is the same constant as in Eq. (22). Similar models of $\delta c(r,z)$ have been used in Ref. [8] where it has been demonstrated numerically that predictions made with the model including $J = 10$ modes closely resemble results observed in field experiments. The model with $J = 1$ in

which the Munk profile is perturbed by a single-mode internal wave has been used in Ref. [9]. In this Section we use model (25) with $J=2$ which is convenient for demonstration of the resonance overlapping phenomenon and its role in the emergence of ray chaos.

The two following sets of amplitudes, A_1 and A_2, have been selected. *Model 1*. $A_1=2.475\times10^{-4}$ km/s, $A_2=4.95\times10^{-4}$ km/s. *Model 2*. $A_1=8.25\times10^{-4}$ km/s, $A_2=16\times10^{-4}$ km/s.

In model 2 the amplitudes are greater by a factor 3.3. All other parameters are the same for both models: λ_j's are some phases, the spatial periods of the perturbation are $L_1=2\pi/k_1=38.16$ km and $L_2=2\pi/k_2=15.9$ km. It should be emphasized that both periods are integer multiples of $L=190.8$ km, i.e., the perturbation is periodic. Surface extrapolated amplitudes of sound-speed fluctuations with range are: $\delta c_{\max}\sim0.3$ m/s in model 1 and $\delta c_{\max}\sim1$ m/s in model 2. These values are typical for real underwater waveguides [8,17].

2. Manifestation of resonance overlapping in phase portraits of rays

If the above perturbations are imposed over a range-independent profile, rays with cycle lengths close to integer multiples of L_1 or L_2 will be captured in resonances. In the right panel of Fig. 1 the cycle length dependencies on launch angle are shown for profiles 1 and 2. Throughout this paper only rays starting from the waveguide axes, i.e., from depths corresponding to minima of sound speed, are considered. We restrict our attention to not very large launch angles. In particular in this section they are taken from the angular interval $(-12°,12°)$. In most real oceanic waveguides such rays play the main role in long-range sound propagation [20]. Steeper rays strike the lossy bottom and substantially attenuate over long propagation distances.

It is easily seen that there will be only one resonance in the waveguide with profile 1, because the corresponding interval of cycle lengths (from 42 to 56 km) contains only one integer multiples of periods of perturbation, namely, $3L_2$. So in this case there is no resonance overlapping.

Profile 2 determines cycle lengths spanning the interval from 25 to 50 km. In this case there will be three resonances centered at rays with the cycle lengths $L_1=38.16$ km, $2L_2=31.8$ km, and $3L_2=47.7$ km. Equation (18) provides estimations of widths of these resonances and then the Chirikov's criterion (24) can be applied to investigate their overlapping. This yields that the resonance centered at a spatial frequency $2\pi/47.7$ km^{-1} remains isolated for both models of the perturbation. The other two resonances overlap. In model 1 we have transition from nonoverlapping to overlapping: the ratios on the right of Eqs. (23) and (24) are slightly less than unity. The Chirikov's criterion is not met for $Q=1$ but it is met for the more realistic value $Q=2/\pi$. In this model we can expect a chaotic behavior of rays with launch angles close to 7°. Trajectories of such rays in phase space lie in the area where the resonances overlap. In model 2 the overlapping is stronger and an interval of launch angles corresponding to rays involved in the chaotic motion is significantly larger than in model 1. Estimations of this interval made with $Q=1$ and $Q=2/\pi$ are of the same order. On the basis of these estimations we expect that rays with launch angles from the interval of about 5° to 8° should exhibit the stochastic instability.

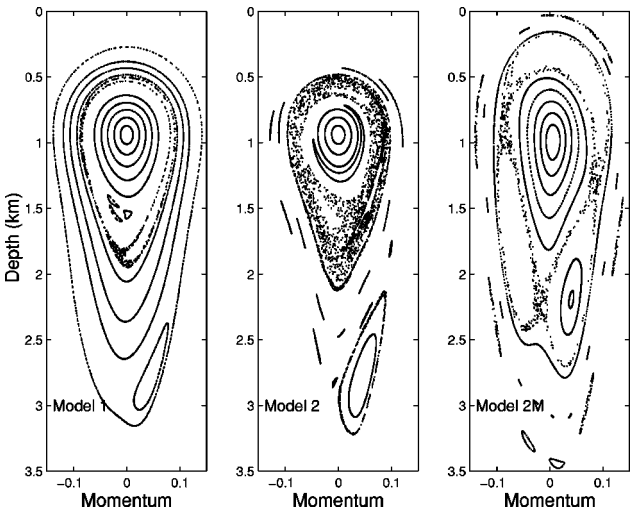

FIG. 3. Left panel: Phase portrait for a waveguide with background profile 2 and model 1 of perturbation. Middle panel: as in the left panel but for model 2 of perturbation. Right panel: as in the middle panel but for background profile 1 (Munk profile).

The chaotic ray behavior can be visualized by the Poincaré map [1–5]

$$(p_{n+1},z_{n+1})=\hat{T}(p_n,z_n), \tag{26}$$

where a symbol $\hat{T}$ denotes transformation of the momentum and coordinate of a ray trajectory taken at a range nL to that at a range $(n+1)L$. Figure 3 presents a set of phase portraits plotted using the Poincaré map. The left panel corresponds to background profile 2 with parameters of perturbation of model 1. This is a set of dots depicting points (p_n,z_n) calculated for 12 rays starting from the depth of 0.94 km (sound-channel axis) at grazing angle 1°,2°, . . . ,12°. Consistent with our expectation, only the ray starting at the angle of 7° exhibits chaotic behavior and produces a thin stochastic layer.

A similar phase portrait for model 2 of perturbation is given in the central panel of Fig. 3. It is clearly seen that the overlapping of resonances gives rise to a significantly stronger chaos. The rays, started at angles of 5°, 6°, 7°, and 8°, belong to the interval covered by overlapping resonances, demonstrate chaotic behavior, and produce a wider stochastic layer compared to that in the left panel. This also agrees with our prediction made on the basis of Eq. (23).

To demonstrate the role of the background profile we consider the same perturbation (model 2) superimposed over profile 1. The phase portrait of the corresponding waveguide is shown in the right panel of Fig. 3. Again 12 rays have been used with take-off angles spaced uniformly from 1° to 12°. This time the starting depth of 1 km (the sound-channel axis for profile 1) has been selected. It is seen that only one ray out of 12 exhibits chaotic behavior. Its launch angle 7° corresponds to a cycle length in the unperturbed waveguide

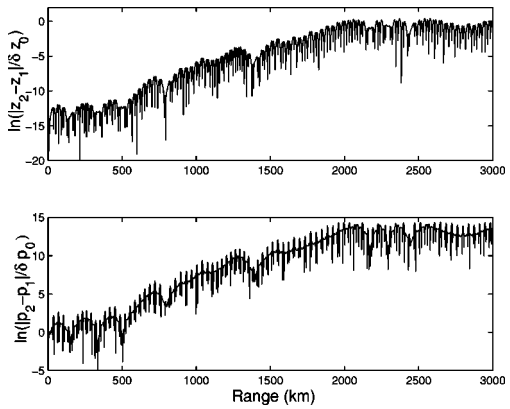

FIG. 4. Differences in depth (upper panel) and momentum (lower panel) versus range for a pair of ray trajectories starting from the point source with close launch angles.

close to $3L_2$, i.e., the stochastic layer in the right panel of Fig. 3 is associated with the presence of a single isolated resonance in this propagation model. As it has been indicated in Sec. II A 4, a thin stochastic layer always exists near separatix of even an isolated resonance.

Comparison of the left and central panels in Fig. 3 shows a quite natural property of ray chaos: the stronger is perturbation, the larger portion of phase space is filled with chaotic rays.

Comparison of the central and right panels demonstrates another feature of chaotic ray dynamics that is less expected: the same perturbation superimposed on seemingly close background profiles gives rise to a strong chaos in one case and a much weaker chaos in another. This phenomenon was first noticed in Ref. [8]. Later on, we interpret it from the viewpoint of resonance overlapping.

3. Stochastic ray instability

The most direct demonstration of stochastic ray motion in model 2 (with the background profile 2) is presented in Fig. 4. Here range dependencies of separations in depth and momentum for two rays starting from the sound-channel axis with slightly different initial momenta are shown. It is seen that both differences, in depth, $\delta z=|z_2-z_1|$, and in momentum, $\delta p=|p_2-p_1|$, for the two rays grow, on average, exponentially with range:

$$|\delta z|\sim e^{\lambda r}, \quad |\delta p|\sim e^{\lambda r}, \tag{27}$$

where λ is the so-called Lyapunov exponent [1]. In the example shown in Fig. 4 $\lambda=1/200$ km^{-1}.

A typical feature of chaotic ray dynamics leading to nonuniformity of the phase space is different sensitivity of trajectories to initial conditions. A convenient tool for identifying regions of ray instability has been used in Ref. [8]. Following this paper we consider the depth difference of the pair of rays whose starting momenta differ only infinitesimally. In other words, we study

$$\delta z(r)=\Lambda_{zp}(r)\,\delta p(0), \tag{28}$$

where

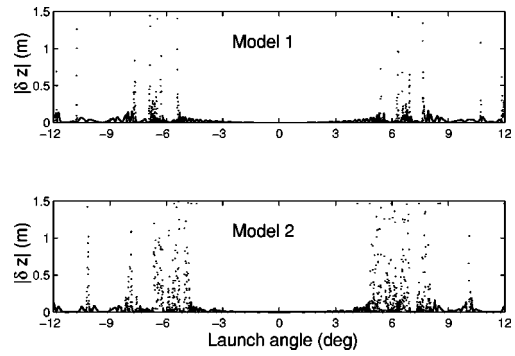

FIG. 5. Depth differences at 1000 km range for pairs of rays with infinitesimally close starting momenta. Each point represents for a given launch angle the absolute difference in arrival depth for two rays: a ray with original momentum and one with a slightly perturbed momentum (which is the original plus 10^{-7}). To construct this plot 4096 pairs of rays were used.

$$\Lambda_{zp}(r)=\left|\frac{\partial z(r)}{\partial p(0)}\right| \tag{29}$$

is one of the main characteristics of local properties of dynamical chaos, and $\delta p(0)$ is an infinitesimal difference in momenta of rays starting from the same point. In our simulation $\delta p(0)=10^{-7}$.

Figure 5 shows the absolute difference, $|\delta z|=|z_1-z_2|$, in arrival depths, z_1 and z_2, of two rays with starting momenta that differ by δp_0 as a function of launch angle at 1000 km range. The calculations have been carried out for the background profile 2. Our objective here is to get some quantitative information on stochastic instability of ray trajectories that reveals itself in appearance of randomly scattered points in the left and central panels of Fig. 3.

The plots demonstrate the intermittent character of zones of high sensitivity. Rays with launch angles between $-5°$ and $5°$ are much less sensitive to inhomogeneities than steeper rays. This fact as well as considerable increase in ray sensitivity to initial conditions in the region of resonance overlapping in model 2, is consistent with the results presented in Fig. 3.

A new property of ray sensitivity dependence on initial conditions, that could not be seen in Fig. 3, is now clearly visible in Fig. 5 (especially in the lower panel). Inside regions of ray instability there are small angular intervals with rather smooth dependence of depth differences on launch angle. This fact suggests that chaotic rays are interspersed with regular ones. In particular, it means that inside stochastic layers observed in Fig. 3 there are numerous ''stable islands'' located in blank spots between the presented points. This situation is general for dynamical chaos [1–5] and it will be discussed more in Sec. III B.

4. Sensitivity of ray travel times

It is natural to expect that stochastic behavior affects any characteristic of ray trajectory. Figure 6 illustrates this statement for ray travel times. This arrival time dependence on launch angle has been computed for 1000 km propagation

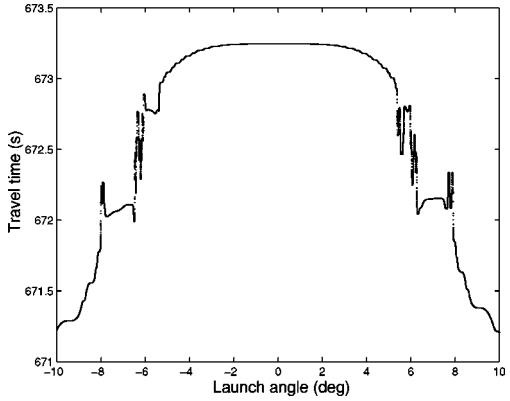

FIG. 6. Ray travel time versus launch angle.

through an ocean-acoustic waveguide modeled by the background profile 2 without (upper panel) and with (lower panel) the model 2 of perturbation (25). 8192 ray trajectories with uniformly incremented starting momenta were evaluated. In accordance with results presented in the middle panel of Fig. 3 and in the lower panel of Fig. 5 most affected are rays with launch angles, $|\alpha_0|$, from about 5° to 8°, i.e., from the angular interval containing most part of chaotic rays. Note that besides randomly scattered points belonging to this interval there are groups of points forming segments of regular curves. This is another manifestation of coexistence of regular and chaotic rays with close initial conditions (see the above comment to Fig. 5).

Figure 7 shows the so-called time front, i.e., a plot representing ray depths against arrival times at the given range. It has been computed for the same set of rays presented in Fig. 6 and every point in the plot represents one ray arrival. Figure 7 illustrates how the chaotic ray motion affects the structure of ray travel times. The chaotic rays with launch angles $5°<|\alpha_0|<8°$ have travel times of about 672 s to 673 s. Comparison of plots in the upper and lower panels of Fig. 7 shows that only segments of the time front corresponding to this interval, i.e., formed by chaotic rays, are significantly

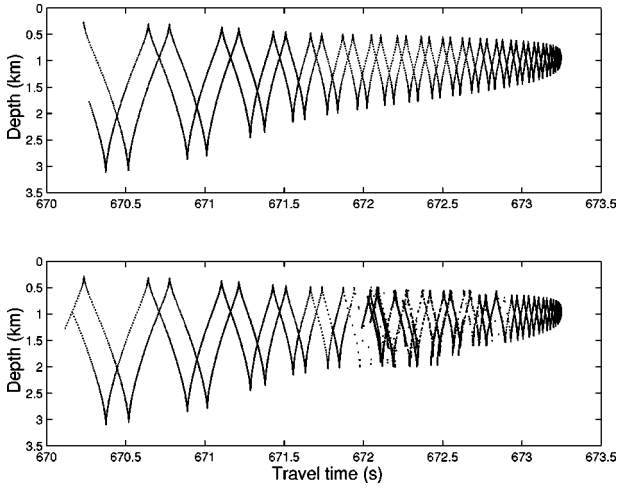

FIG. 7. Time fronts for a waveguide without (upper panel) and with (lower panel) model 2 of perturbations. Background profile 2 was used.

distorted in the presence of perturbation.

Stochastic properties of ray travel times will be investigated in more detail in the following section for another model revealing a more strong ray chaos.

5. Ray sensitivity to the background profile

Numerical results presented in this section shows that the phenomenon of ray-medium resonance should play a significant role in underwater acoustic waveguides. In particular, considering of this phenomenon may shed an additional light on the effect noticed in Ref. [8]. In that paper it has been demonstrated numerically that the same weak range-dependent inhomogeneities placed in waveguides with different background sound-speed profiles lead to different chaotic properties of ray structure. The authors argue that the curvature at the sound-channel axis strongly influences the character of the ray behavior: the stronger the curvature the more chaotic ray motion is. This statement agrees with our results presented above. Our background profile 2 has a greater curvature than profile 1, and comparison of the phase portraits in the central and right panels of Figs. 3 shows that in the waveguide with profile 2 ray chaos is stronger. To give some explanation to a similar effect, the authors of Ref. [8] refer to results of Duda and Bowlin [21] who argue that a normalized sound-speed curvature strongly controls caustic formation.

Bearing in mind the role of ray-medium resonance in emergence of chaos, we can interpret this in a following viewpoint. Note, that a large curvature corresponds to a strong dependence of the trajectory cycle length on the launch angle. For example, compare the two curves shown in the right panel of Fig. 1. The cycle lengths corresponding to profile 2 (large curvature) span the interval of almost twice the size of that corresponding to profile 1 (small curvature). Correspondingly, the interval of spatial frequencies ω for profile 2 is also two times wider compared to profile 1. In the limiting case of a profile with an infinite curvature (e.g., a bilinear sound-speed profile), the interval of spatial frequencies becomes infinite because in this case the interval of cycle lengths begins from zero [22].

On the other hand, it is clear that the larger is an interval of cycle lengths, more are chances for ray trajectories to be in resonance with some harmonics of the perturbation and, hence, more chances exist for resonance overlapping and giving rise to strong ray chaos.

III. TRAVEL TIME OF CHAOTIC AND REGULAR RAYS

A. Description of the model

Our primary concern in this section is with chaotic properties of ray travel times. In many schemes of acoustic monitoring of ocean structure these parameters are main observables used for solving inverse problems [10].

Following Refs. [5,18] we consider here wave propagation in the canonical Munk waveguide (profile 1 in Fig. 1) given by Eq. (22) with a perturbation

$$\delta c(r,z)=2\gamma c_0 z/Be^{-2z/B}\cos(2\pi r/\lambda), \qquad (30)$$

where $\gamma = 0.01$ and the spatial period $\lambda = 10$ km. The amplitude of δc takes its maximum value of about 5 m/s at 500 m depth. Note that this perturbation is significantly stronger compared to models considered in the preceding section and chaotic properties of ray travel times that we are going to discuss are here more pronounced.

1. Phase portrait

A phase portrait of ray motion for the model defined by Eqs. (22) and (30) is shown in Fig. 8(a). Here we have used Poincaré map (26) with sections spaced apart by λ. Although the perturbation is now stronger, coexistence of regular and chaotic trajectories persists. This fundamental property of Hamiltonian dynamics follows from the Kolmogorov-Arnold-Moser theory [16] and does not depend on how small or strong the perturbation is. However, the portion of the phase space occupied by regular trajectories usually decreases with the magnitude of perturbation. Comparison of phase portraits presented in Figs. 3 and 8(a) illustrates this statement.

The phase portrait in Fig. 8(a) presents a familiar picture of ''stable islands'' filled with regular curves in the ''chaotic sea'' filled with randomly scattered points. The largest island in the center of Fig. 8(a) is formed by rays propagating at small grazing angles. These rays are regular and it is natural to expect that their contributions should form a regular part of the time front. Numerical results presented below are consistent with this expectation.

An important feature of chaotic behavior of the ray trajectory in the chaotic sea is the so-called stickiness, i.e., the presence of such parts in a chaotic trajectory where the latter exhibits an almost regular behavior. This occurs when after wandering in the phase space the trajectory approaches a stable island and ''sticks'' to its border for some time that may be fairly long [23]. This phenomenon reveals itself in Fig. 8(b) where the Poincaré map (26) of a single ray starting from 1 km depth with an initial momentum $p_0 = -0.137\,893$. The density of points depicting the trajectory is most high in the vicinity of five islands (surrounding the large island in the center) that we have already seen in Fig. 8(a). It means that this particular trajectory sticks to these islands.

2. Chaotic sea as a result of resonance overlapping

This phase portrait can be interpreted from the viewpoint of resonance overlapping discussed in Sec. II. Equation (16) defining resonant values of the action for model (30) translates to

$$m\,\omega(I) = 2\pi/\lambda. \tag{31}$$

The function $\omega(I)$ for the Munk profile is shown in Fig. 2(a). Ray trajectories (on the phase plane) in the unperturbed waveguide corresponding to the resonant values of I are shown in Fig. 8(c) by thick-solid lines. They are superimposed on the Poincaré map, the same as in Fig. 8(a). The trajectories with larger values of I embrace trajectories

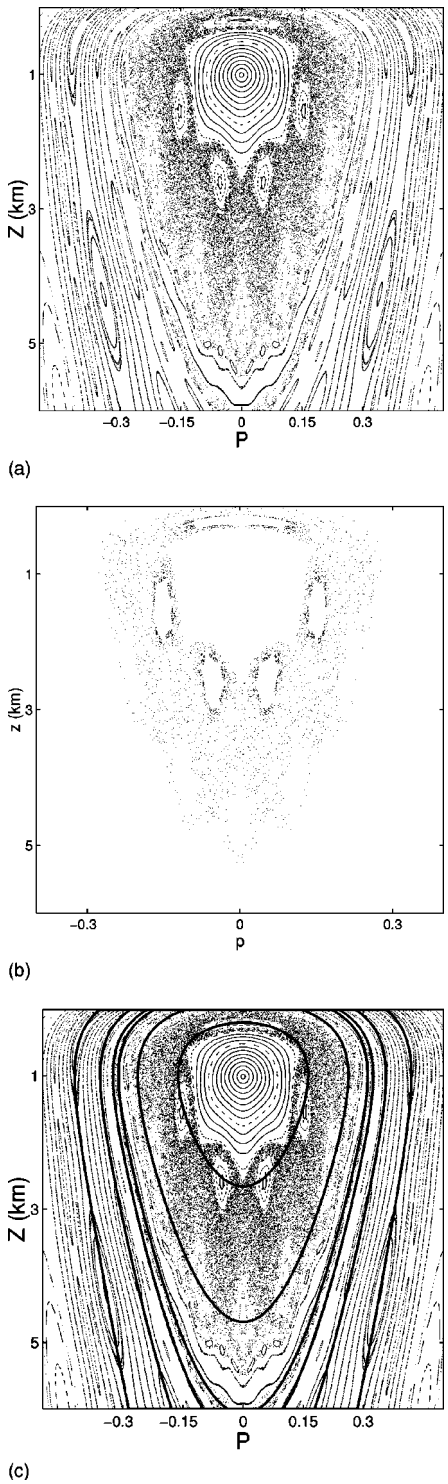

FIG. 8. Poincaré maps of rays in the waveguide with the Munk profile and the perturbation given in Eq. (30). (a) Phase portrait of a field excited by a point source set at 1 km depth. (b) Phase portrait of a single ray starting at 1 km depth with the momentum $p_0 = -0.137\,892$. (c) Resonant ray trajectories in the unperturbed waveguide superimposed on the phase portrait constructed for the perturbed waveguide (the same map as in upper panel). Trajectories corresponding to larger values of action embrace that corresponding to smaller values of action.

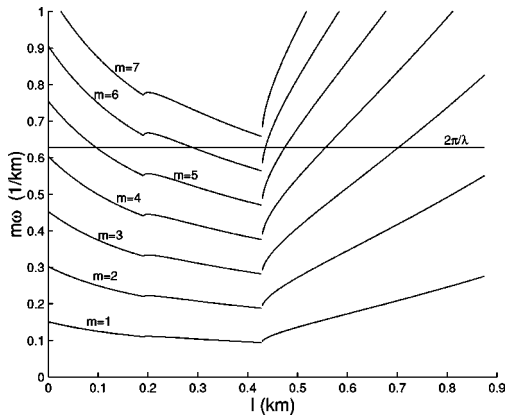

FIG. 9. Dependencies of $m\omega(I)$ on the action variable I for the unperturbed Munk profile ($m=1,2\ldots,7$).

corresponding to smaller values. The resonant values of I have been found by solving Eq. (31) as it is illustrated in Fig. 9. The straight horizontal line in Fig. 9 indicates the angular frequency of the perturbation (30), $2\pi/\lambda$. Intersections of this line with other curves depicting the functions $m\omega(I)$ for different integer m, occur at resonant values of the action I satisfying condition (31).

To make some conclusion on resonance overlapping we have estimated resonance widths in terms of action using Eq. (17). This estimation shows that the large chaotic area in the Poincaré map is a result of overlapping of the first two resonances corresponding to two innermost solid curves in Fig. 8(c). All the other resonances do not overlap. However, it should be mentioned that the perturbation theory described in Sec. II A 3 is here of limited use. The point is that the parameter ε defined in Eq. (19) for perturbation (31) is about 0.1. For $I<0.45$ km this value is not small compared to α [see Figs. 2(c) and 2(d)] as it is required by the left inequality in Eq. (20). This inequality completely fails near $I=0.2$ km where α vanishes. Nevertheless, we see that the overlapping criterion (24) gives a reasonable prediction of the area of the phase plane occupied by chaotic sea.

3. Diffusion of action

The Poincaré map presented in Fig. 8(a) shows that rays starting from a point source located at 1 km depth with starting momenta from the interval $0.13<|p_0|<0.28$ should be predominantly chaotic and wander inside the chaotic layer, i.e., within the area in Fig. 8(a) formed by randomly scattered points. Here we are studying stochastic range variations of action variables of these rays. The limiting values of actions corresponding to boundaries of the chaotic layer can be approximately estimated as $I_{\min}=0.06$ km and $I_{\max}=0.35$ km.

Figure 10(a) presents the difference in action variables against range for two trajectories starting from 1 km depth with the slightly different initial momenta: $p_0=0.19$ and $p_0=0.190\,01$. It is clearly seen that up to 1000 km range the difference grows, on average, exponentially and the inverse Lyapunov exponent $\lambda^{-1}=120$ km. Beyond 1000 km range the difference becomes of order of $I_{\max}-I_{\min}$ and then it saturates.

In Fig. 10(b) range dependencies of actions for 500 rays starting at 1 km depth with initial momenta spaced uniformly within the interval from 0.2 to 0.205 are shown. It is clearly seen how this bunch of trajectories is widening with range until, at about 700 km, it fills the whole space between $I_{\min}$ and $I_{\max}$. At longer ranges the width of the bunch remains constant, approximately equal to $I_{\max}-I_{\min}$. Figure 10(b) gives a visual representation of diffusion of action.

B. Chaotic wave transmission

Finiteness of the waveguide length leads to the problem called in Ref. [18] the problem of ''chaotic transmission.'' The origin of this phenomenon lies in nonuniformity of the phase space. The latter is not ergodic and different rays have different fractal properties depending on propagation range.

The Poincaré map constructed by means of ray trajectories evaluation at very long ranges, allows one to understand which parts of the phase space are filled with regular or chaotic rays. But ranges of real interests for underwater acoustic are not very large. Acoustic paths lengths in experiments on long-range sound propagation vary from a few hundreds to a few thousands kilometer [10,12]. A typical cycle length of ray trajectory oscillations is of order of a few dozens kilometer [20,22]. It means that the number of oscillations seldom exceeds 150–200 and in many experiments is only of order of ten. Therefore some trajectories with starting parameters belonging to the ''chaotic sea'' have no chance to exhibit chaotic behavior at real acoustic paths.

This point is illustrated in Fig. 11 where the ray travel time is plotted against the starting momentum at ranges of 1500, 3000, and 5000 km. Three successive magnifications

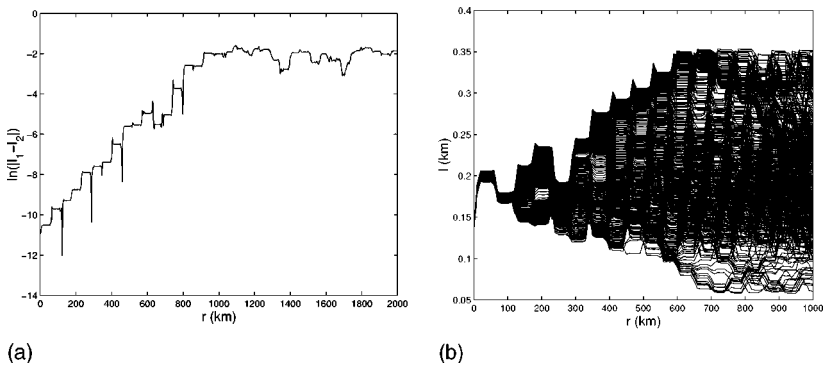

(a) (b)

FIG. 10. Diffusion of actions in the perturbed Munk profile. (a) Difference in action variables, I_1 and I_2, for two trajectories starting from 1 km depth with initial momenta 0.19 and 0.190 01. (b) Bunch of 500 ray trajectories with starting momenta equally spaced within the interval from 0.2 to 0.205.

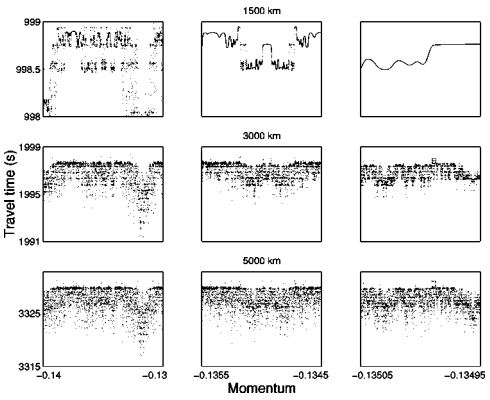

FIG. 11. Travel times versus starting momentum at ranges of 1500 km (upper row), 3000 km (middle row), and 5000 km (lower row). The plots in each column corresponds to the same interval of starting momenta.

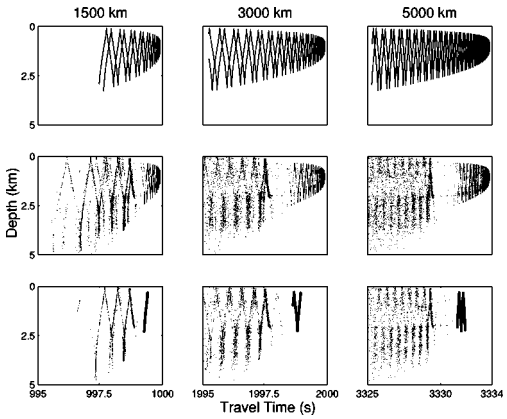

FIG. 12. Time fronts at 1500 km (left column), 3000 km (middle column), and 5000 km (right column) in the unperturbed (upper row) and perturbed (middle row) waveguides. The lower row of plot represents results computed for fans of rays from a narrow interval of starting momenta ($-0.14<p_0<-0.13$). Points represent ray arrivals in the perturbed waveguide, thick-solid lines represent arrivals in the unperturbed waveguide.

of this dependence are shown for each range. At 1500 km the randomly scattered points are interspersed with segments of regular curves. At longer ranges the magnification by a factor of 100 does not reveal smooth curves.

This situation is similar to that encountered in the problem of chaotic scattering [24]. In the chaotic transmission problem an inhomogeneous waveguide plays the role of the chaotic scatterer, and characteristics of this scatterer depend not only on inhomogeneities but on range as well.

It should be emphasized that different ray trajectories have different asymptotes at long range. This important aspect of the chaotic transmission phenomenon is connected to the stickiness. This phenomenon, shortly discussed in Sec. III A 1 and illustrated in Fig. 8(b), leads to appearance of long almost regular portions of a chaotic trajectory when the trajectory sticks to borders of some stable islands.

If the trajectories of the problem follow the Gaussian type process then their distribution can be described by a diffusion type equation with uniform asymptotes at $r \gg r_{dif}$, where r_{dif} is the diffusional length. However, the presence of islands changes the uniformity property so that different bunches of rays can have different intermediate asymptotes at long ranges. The role of islands is crucial for the appearance of jets of almost coherently propagating trajectories (from the chaotic sea) that can occur and survive at very long acoustic paths. The concept of chaotic transmission has been introduced to attract the attention to the fact that even chaotic rays can be distinguished by their different asymptotic behavior as a result of the non-Gaussian character of chaotic dynamics.

C. Timefronts for unperturbed and perturbed waveguides

1. Range dependence of the time front

Figure 12 presents time fronts at three different ranges computed for a point source located at 1 km depth, i.e., at the axis of the unperturbed sound-speed profile. Starting momenta, p_0, of sample rays have been uniformly distributed over the interval $-0.2 \leqslant p_0 \leqslant 0.2$. The corresponding interval of launch angles spans from $-11.5°$ to $11.5°$. The latest part of the arrival pattern is formed by axial rays that, as we already know, remain regular in the presence of perturbation (30). So, it is not surprising that axial tails of arrival patterns in the perturbed and unperturbed waveguides (cf. upper and middle rows of plots in Fig. 12) look very much alike. Much more surprising is that the earlier portion of the time front produced by chaotic rays remains, to some extent, similar to that in the unperturbed waveguide. Let us discuss this point in more detail.

When the perturbation is absent, the time front has the folded accordion shape and consists of segments of smooth lines (see the upper row of plots in Fig. 12). Each segment is formed by rays with the same identifier $J=\pm N$, where $\pm$ is the sign of the launch angle and N is the number of ray turning points (i.e., points of the trajectory where the grazing angle changes sign). Rays with the identifiers $+N$ and $-N$ produce two neighboring intersecting segments. Rays with positive and negative identifiers form two piecewise lines of accordionlike shape with some relative shift along the time axis.

This property remains valid for chaotic rays. This is illustrated in Fig. 13 where magnified fragments of two time-fronts from Fig. 12 computed for 3000 km range are presented in the same plot. All arrivals with $J=-115$ and $J=-116$ are shown for both perturbed and unperturbed waveguides. Crosses and asterisks depicting arrivals in the range-independent model form two smooth segments. Points and circles depicting arrivals with the same identifiers in the perturbed waveguide form two sets of randomly scattered points in the neighborhood of two similar smooth segments. Loosely, chaotic rays produce a dispersed version of the pattern typical of the range-independent waveguide.

Another manifestation of this property of ray dynamics in range-dependent waveguides was demonstrated in Ref. [7], where properties of eigenrays, that is, the rays that pass through the given point of the waveguide, were studied numerically. It turned out that groups of chaotic eigenrays with the same identifier tend to form clusters of arrivals with sur-

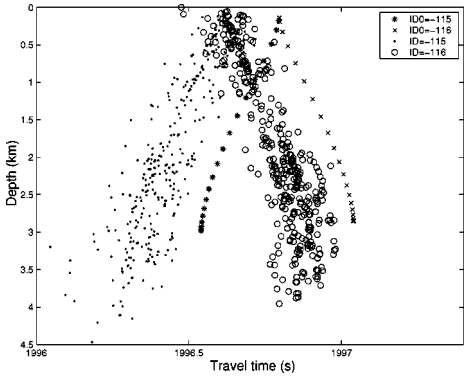

FIG. 13. Fragments of the time fronts at 3000 km range formed by rays with identifiers equal to -115 and -116 in the perturbed (points and circles) and unperturbed (asterisks and crosses).

prisingly small time spreading within each cluster. Looking at Fig. 13 we see that in our case this property of eigenrays should also take place. Indeed, it is natural to expect that all the eigenrays at 3000 km range arriving at a depth of, say, 2.5 km with identifier -115 will be located at a segment of horizontal line $z=2.5$ km inside the area filled with circles. A time spread of this cluster will be about 0.25 s and there will be no overlapping with neighboring clusters.

The lowermost row of plots in Fig. 12 presents contributions to the above time fronts from rays with starting momenta p_0 from a narrow interval $-0.14 \leqslant p_0 \leqslant -0.13$ that corresponds to launch angles from $-8.3°$ to $-7.45°$. These plots demonstrate a great difference between regular (thick-solid lines) and chaotic (scattered points) time fronts. In the range-independent waveguide arrivals are spread in a smooth and predictable way and cover one or two (depending on range) segments of the time front depicted by solid lines.

In the presence of perturbation arrivals of rays with the same starting momenta are spread over several segments of the time front. It should be emphasized that chaotic nature of their dynamics reveals itself in the fact that rays with close starting parameters ''jump'' to different segments in a random manner. This situation is in sheer contrast with that in the unperturbed waveguide, where trajectories with the same identifier have starting momenta within a fixed angular interval and rays with starting momenta outside this interval have different identifiers.

2. Fractal properties of the time front fine structure

Fractal properties of rays can be characterized in different ways. Here we restrict our attention to the ray travel time and examine the same interval of starting momenta, $-0.14 < p_0 < -0.13$ presented in Fig. 11 and in the lower row of plots in Fig. 12. As it has been already mentioned, the magnification presented in Fig. 11 do not reveal a smooth curve in the travel time dependence on the starting momentum at 3000 and 5000 km ranges. It suggests that the function under consideration has a fractal structure.

To obtain a quantitative characteristic of this structure we have computed ''lengths'' L of curves that can be constructed by connecting points presented in the left column of plots in Fig. 11. The ''length'' L has been defined as the sum

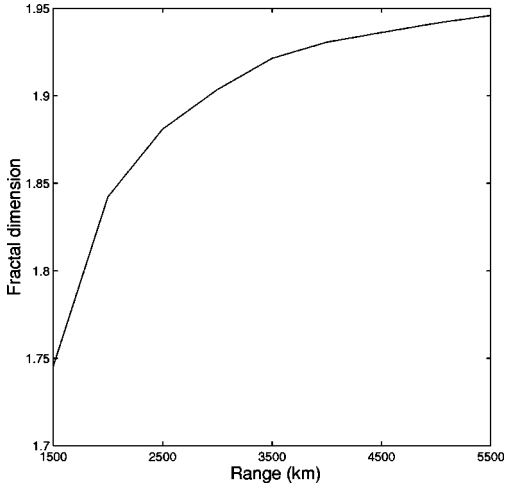

FIG. 14. Fractal dimension of travel time dependence on starting momentum as a function of range.

$$L(\Delta) = \sum_i |t_{i+1} - t_i|, \tag{32}$$

with t_i being travel times of rays with starting momenta $p_{0,i}$ uniformly spaced apart by Δ $(p_{0,i+1} - p_{0,i} = \Delta)$ over the interval $-0.14 \leqslant p_{0,i} \leqslant -0.13$. The computations have shown that $L \sim \Delta^{-d}$, were d is some positive constant from the interval $1 < d < 2$. It confirms our assumption about a fractal structure of the timefront. The constant d is a fractal dimension and its range dependence is shown in Fig. 14.

D. Travel time gap

An interesting and somewhat unexpected feature of the time fronts depicted in the middle row of plots in Fig. 12 is the presence of gaps between travel times of regular and chaotic rays. These gaps are also clearly seen in Fig. 15 where travel time dependencies on starting momenta and histograms (relative number of arrivals per a small fixed time interval) representing travel time distributions are shown.

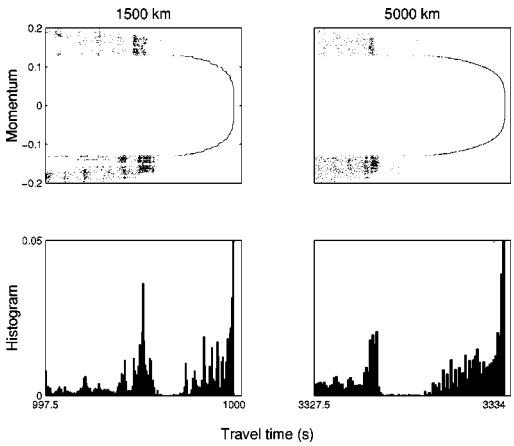

FIG. 15. Upper row: travel time versus starting momenta. Lower row: histogram of ray travel times.

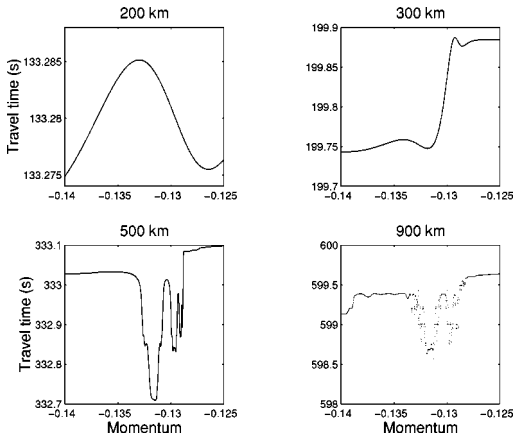

FIG. 16. Travel time as a function of starting momentum at four different ranges.

Note, that in the unperturbed waveguide (see the upper row of plots in Fig. 12) the ray travel time are spread in a smooth way without any gaps.

A qualitative explanation of this effect is as follows. In range-independent waveguides with sound-speed profiles like those presented in Fig. 1 signals propagating through near-axial rays arrive at the given range later than signals going through steep rays. It is a typical feature of underwater acoustic waveguides [8,12]. The point is that most parts of steep ray paths lie far from the sound-channel axis, i.e., in water layers with comparatively large sound speeds. Therefore in the range-independent waveguide the travel time t at the given range decreases with $|\alpha_0|$, where α_0 is the launch angle.

The presence of perturbation changes the situation. In the phase plane shown in Fig. 8(a) the starting positions of rays emitted by a point source at 1 km depth lie on the straight line $z=1$ km. Rays with starting momenta $|p_0|<0.13$ ($|\alpha_0|<7.45°$) belong to the stable island. They are regular and form axial tails in the chaotic time fronts that are very close to corresponding parts of regular time fronts shown in the upper row of plots in Fig. 12. But this is no longer true of rays with $|p_0|>0.13$ ($|\alpha_0|>7.45°$), i.e., with starting parameters from speckled regions of "chaotic sea." Beyond this border we are entering an interval corresponding to predominantly chaotic rays. The latter have trajectories sampling larger depth intervals compared to that of unperturbed rays with the same launch angles. Therefore an averaged sound speed over the chaotic ray path is greater than that for the unperturbed regular ray with the same initial conditions. This causes decrease of arrival times of chaotic rays. In this sense, the existence of the gap is a consequence of a sharp boundary between initial conditions of chaotic and regular rays. It should be pointed out that the gap is not empty, but the density of arrivals inside this area is much less than in neighboring parts of the time front.

Studying of evolution of the travel time dependence on the starting momentum with distance shows that the gap appears already at ranges of a few hundred kilometers. It is seen in Fig. 16, where plots depicting travel times versus starting momenta are shown for several ranges. The gap appears already at 300 km range.

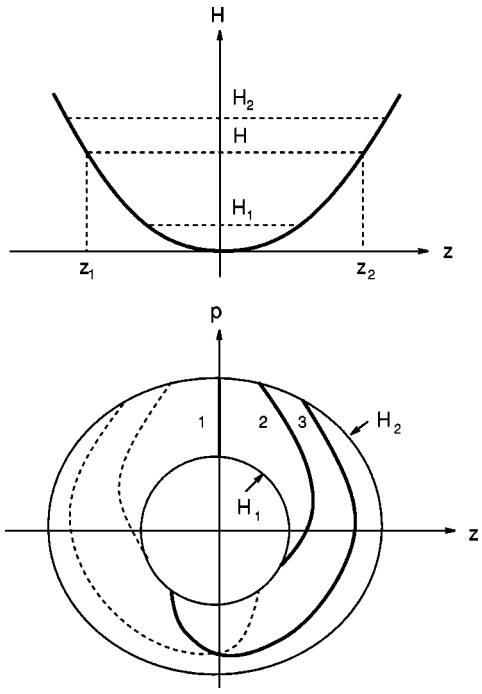

FIG. 17. Upper panel: Typical dependence of the Hamiltonian H on depth, z. Lower panel: Plot schematically representing wave-front variations with range. Thick solid and dashed curves depict wave fronts corresponding to rays with starting momenta of different signs.

A more detailed investigation of characteristics of the gap and their dependence on the parameters of the problem will be considered elsewhere. Here we just notice that in the time front computed for the model considered in the preceding section and shown in Fig. 7 the gap is not so apparent as in Fig. 12. Nevertheless we can see a comparatively low density of arrivals at times of about 672 s. This is also seen in the travel time dependence on the launch angle presented in Fig. 7. This portion of the time front is formed by rays with launch angles close to 8°. As we know, this angle corresponds to one of the two borders between regular and chaotic rays. At the other border, corresponding to starting angles of about 5° and travel times of about 672.9 s, the gap is practically absent.

IV. RAY CHAOS IDENTIFICATION

This section consists of the main conclusive theoretical part of the article: identification of presence the chaotic/nonchaotic rays on the basis of the analysis of the time front distributions. We shall start from an auxiliary material.

A. Phase diagram and wave-front evolution

Let us come back to the Munk profile (22) for the potential of the ray dynamics. For a given "energy" H a ray "particle" bounces between points (z_1,z_2) as it is shown in the upper panel of Fig. 17. The spatial frequency of the bounces (oscillations) is

$$\omega(H)=\frac{dH(I)}{dI}>0, \tag{33}$$

while its derivative is negative

$$\frac{d\omega(I)}{dI}=\omega(H)\frac{d\omega(H)}{dH}=\frac{d^2H(I)}{dI^2}<0 \tag{34}$$

as it follows from Fig. 2(b) for the main part of the interval of accessible values of I or H. In Eqs. (33) and (34) we consider dependence of ω on H instead of the action I. It follows from Eq. (34) that the larger (or higher) is the energy level H in the upper panel of Fig. 17, the greater is the interval of bounces of a ray (z_1,z_2) and the longer is the spatial cycle (period of oscillations). At the same time, the mean sound speed increases with the growth of H. On phase plane (z,p) an unperturbed ray trajectory is a circle (lower panel of Fig. 17). The distribution of ray depths taken at the same range in the lower panel of Fig. 17 will be called *"phase diagram."* Consider now all trajectories that have values of the energy H in the interval (H_1,H_2) and the same value $z=z_0$ at the range $r_1=0$. The thick line that connects on the *phase diagram* all positions of rays with different value of their momenta and energies but with the same range r is called the *wave front*, i.e., phase diagram provides a wave front on phase plane. In the lower panel of Fig. 17 we show by thick lines three wave-fronts locations at ranges $r_1=0$, $r_2>0$, and $r_3>r_2$. They are parts of the *front spirals* that rotate clockwise. By thick-dash curves we show similar wave fronts that rotate counterclockwise. Each time when the spiral acquires a full circle, the wave front in the phase diagram gains more multiplicity values. It corresponds to appearance of two more breaking points in unperturbed time fronts like those shown in Fig. 12 (top row) or Fig. 7 (top). Dash-curves wave fronts are similar to the described ones but slightly different since the potential shape in the upper panel of Fig. 17 is asymmetric. The outer points of the front are closer to final point since they move slower than internal points due to Eq. (34). The described way of the wave-front evolution on phase diagram is equivalent to the wave-front observation data as it is shown in Fig. 7 (top).

Let us consider arrival time $t(L,H)$ depending on the position of a point on the phase diagram. For the fixed L and H it follows from Eqs. (4) and (10)

$$t(L,H)=\frac{1}{c_0}\left\{\int_0^L p\,dz-HL\right\}=\frac{L}{c_0}(I\omega-H). \tag{35}$$

After differentiation of Eq. (35) with respect to I and applying Eq. (14) we obtain

$$\frac{dt(L,H)}{dI}=\frac{L}{c_0}I\frac{d\omega}{dI}. \tag{36}$$

In correspondence to Eq. (34)

$$dt(L,H)/dI<0$$

meaning that the larger is I, i.e., the larger is H, the smaller is arrival time. In other words the higher is a ray trajectory cycle in the upper panel of Fig. 17, the faster a signal propagates along this ray.

Now let us add a perturbation.

B. Stochastic ray acceleration

Consider the energy H_c (action I_c) corresponding to the boundary of the stable island on phase plane. It follows from the overlapping criteria (24) that chaotic dynamics occurs in a domain $H>H_c$ $(I>I_c)$ or $\omega<\omega_c\equiv\omega(H_c)$. More precisely, dependence of the frequency $\omega(H)$ on H (or I) is not monotonic as it follows from Fig. 2. That makes a possibility of chaotic dynamics in a finite domain $H_c<H<H_{\max}$ or $I_c<I<I_{\max}$. A possible situation of a localized chaos is shown in Fig. 8(c) where the strong chaotic behavior is limited by the central island, i.e., H_c (or I_c), and by some outer value $H_{\max}$ or $I_{\max}$.

The dynamics in the stochastic sea can be presented in different ways and one of them is to consider an arrival time $t(L,H_0)$ with an initial energy $H_0>H_c$ as a sum of slightly correlated additives

$$t(L,H_0)=\sum_{j=1}^{\nu}\Delta t_j(H_j,L), \tag{37}$$

where Δt_j is a propagation time over a cycle

$$\Delta L_j=2\pi/\omega(E_j) \tag{38}$$

of two full bounces of a ray in Fig. 12. We assume that the energy E_j of the ray does not change its value along the range interval ΔL_j and

$$\sum_{j=1}^{\nu}\Delta L_j=L. \tag{39}$$

The chaotic ray dynamics means that due to the large number law,

$$\sum_{j=1}^{\nu}\Delta L_j\approx\nu\langle\Delta L\rangle=L \tag{40}$$

and

$$\sum_{j=1}^{\nu}\langle(\Delta L_j-\langle\Delta L\rangle)^2\rangle\sim\nu\langle(\Delta L)^2\rangle \tag{41}$$

if $\nu\gg1$. Consequently, the distribution function for ΔL_j is focused close to the value

$$\Delta L_0\sim\Delta L(H_0),\quad H_0=(H_{\max}-H_c)/2 \tag{42}$$

and its width can be of order $\Delta L_0/\nu^{1/2}$. In Sec. V we shall see that chaotic behavior of near-axial rays due to mesoscale inhomogeneities may require a different method of description and in this case relations (37)–(42) need some modification.

As a result of this consideration, we can conclude that a ray with a starting energy close to H_c propagates in the stochastic sea area in such a way that its energy H grows from H_c to the value $H_{\max}$ with a maximum of the distribution function somewhere at $H_0 > H_c$. It follows from the preceding Sec. IV A that a ray with $H > H_c$ has a shorter arrival time. In analogy to the so-called stochastic particle acceleration [15] this phenomenon can be named *stochastic ray acceleration*.

Criterion of chaos (24) is valid for the domain outside of the large island in the center of Fig. 8(a). Rays (particles) diffuse outside into the direction corresponding to actions I greater than I_c. This yields a gap in ray intensities (numbers of rays) at I near I_c. That is exactly what is observed in Fig. 12: the gap in the number of rays for the same interval of actions leads to a gap in travel time distribution since chaotic rays are accelerated compared to nonchaotic rays.

C. Diagnostics of ray chaos

Here we would like to formulate what kind of properties of the time front are responsible for the chaotic ray dynamics and how one can identify the phenomenon of chaos.

1. Time front gap

Appearance of the gap in the time front indicates the presence of chaotic rays. Moreover, other types of weaker gaps can appear at shorter arrival times.

2. A maximum in the arrival time distribution

A maximum of the number of the arrival rays appears right before the arrival gap (Fig. 15, lower row). We suppose that the presence of this maximum is related to the phenomenon of stickiness [23,25] to the first resonance islands set in the domain of the chaotic dynamics. The stickiness to the corresponding set of islands can be also seen from the Fig. 8(c) of the phase plane. The sticky trajectories perform almost regular dynamics without escape to the stochastic sea for a fairly long time. As a result, an analog to the stochastic acceleration is declined and a local maximum appears in the arrival time distribution. However, the issue of manifestation of the stickiness in ray travel time distribution requires a further investigation.

3. Fuzziness and the front splitting

As it is seen from Fig. 12 (middle and lower rows) there is a tendency of splitting of fronts into few close fronts with a simultaneous fuzziness of the front structure. Typically, chaos occurrence can be interpreted as the strong phase mixing. We mean the phase of the ray trajectory represented by the angle variable, θ. As a result, clockwise moving set of fronts and counterclockwise moving set can intersect each other at the same phase point what is impossible for regular dynamics without special conditions. This intersection provides occurrence of satellite fronts after a shorter time (range) than without chaos.

4. Phase jump

Another manifestation of the strong phase mixing is seen in Fig. 14 in extreme sensitivity of the number of turning points to the starting momentum. The jumps in number of turning points means *phase jumps*, i.e., jumps of the angle variable θ, of order 2π. These irregular jumps lead to irregularity of the time front in perturbed waveguides (see Figs. 7 and 12). An interesting and surprising phenomenon is that in spite of these random jumps, some regular structures are apparent in the time front. In the presence of perturbation we see a fuzzy version of the accordionlike shape of the time front typical of an unperturbed waveguide. A similar stability of portions of the time fronts formed by steep rays has been observed in numerical simulations [8] and field experiments [12].

V. CHAOTIC RAY DYNAMICS IN A DEEP SEA WAVEGUIDE WITH MESOSCALE INHOMOGENEITIES

Although there are a variety of factors affecting long-range sound transmission through the real ocean, in underwater acoustics it is believed that in many cases the fluctuations of the signal propagating in the deep sea at a carrier frequency of order 100 Hz are mainly determined by sound-speed variations induced by (i) internal waves and (ii) mesoscale inhomogeneities [13,17,26].

The internal waves are characterized by horizontal spatial scales ranging from hundreds of meters to tens of kilometers and vertical scales of tens of meters. Their temporal scales are on the order of hours. The word mesoscale denotes sound-speed inhomogeneities whose horizontal scales range from tens to hundreds kilometers, and which evolve on time scales of one month. The corresponding vertical scales are from 100 m to 1 km [27].

The idealized environmental models discussed in the preceding sections are aimed at studying internal-waves related mechanisms of stochastic ray instability. In contrast, in the present section we focus on ray behavior in the environment with mesoscale range variations and demonstrate numerically that even in the absence of internal waves, these inhomogeneities alone can give rise to ray chaos. On the other hand, it turns out that there exists a difference between mechanisms leading to chaotic ray dynamics for the two types of inhomogeneities.

A. Ocean mesoscale variability measured during the acoustic engineering test

A particular model of the deep see environment used in this section has been constructed on the basis of real hydrographic data (combined with the historical data) measured in the North Pacific Ocean in 1994 during the acoustic engineering test (AET) [12,13]. In this experiment sound transmission over 3000 km range was investigated and the nearly concurrent temperature and salinity measurement were carried out along the acoustic paths. Much of the variability produced by internal waves has been smoothed out from the hydrographic data and after some processing the model of sound-speed field with mesoscale spatial variations was ob-

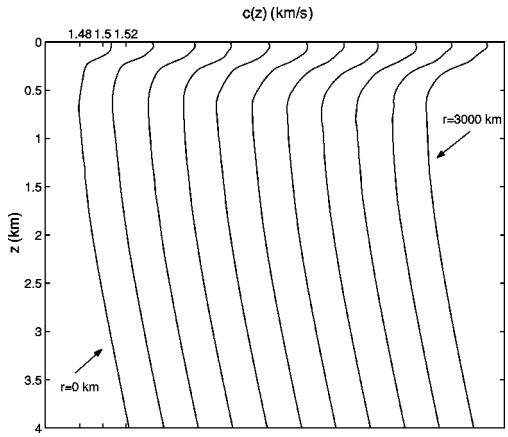

FIG. 18. Sound speed profiles at 3000 km range. Profiles are plotted every 300 km with a sound-speed offset 0.2 km/s.

tained. This model representing typical features of the deep sea acoustic waveguide, has been used in our numerical simulations described below.

The sound-speed profile evolution within 3000 km range interval is shown in Fig. 18. Note that the depth of the sound-channel axis (the minimum of the sound-speed profile) is gradually increasing with range. In this figure, we see only largescale features of the sound-speed field while the details with lesser spatial scales, are not discernible. It is well known that most of the small-scale variability in the environment occurs in the upper part of the waveguide, near or above the sound-channel axis [17,22]. A detailed visualization of the refractive index variability at depths ranging from $z=0$ km (sea surface) to $z=1$ km is presented in Fig. 19. In this figure, local extrema of the refractive index spread in an irregular way are clearly seen at depths of 500–800 m.

Although the sound-speed fluctuations in the vicinity of the sound-channel axis are rather small (0.1–0.5 m/s), they can strongly affect near-axial rays propagating at small grazing angles. For these rays $|p| \ll n \approx 1$ and the Hamiltonian (2) can be approximated by [1,2]

$$H = \frac{p^2}{2} + U(r,z) \tag{43}$$

with the ''potential''

$$U(r,z) = [1 - n^2(r,z)]/2. \tag{44}$$

At each cross section of the waveguide, U as a function of z has a shape of some potential well with a minimum at the sound-channel axis. Due to the mesoscale inhomogeneities this minimum is not sharply defined. Moreover, at small values of U usually there are a few local minima. Each minimum forms a local waveguide channel and, as we shall see below, ray trajectories can be trapped in such microchannels.

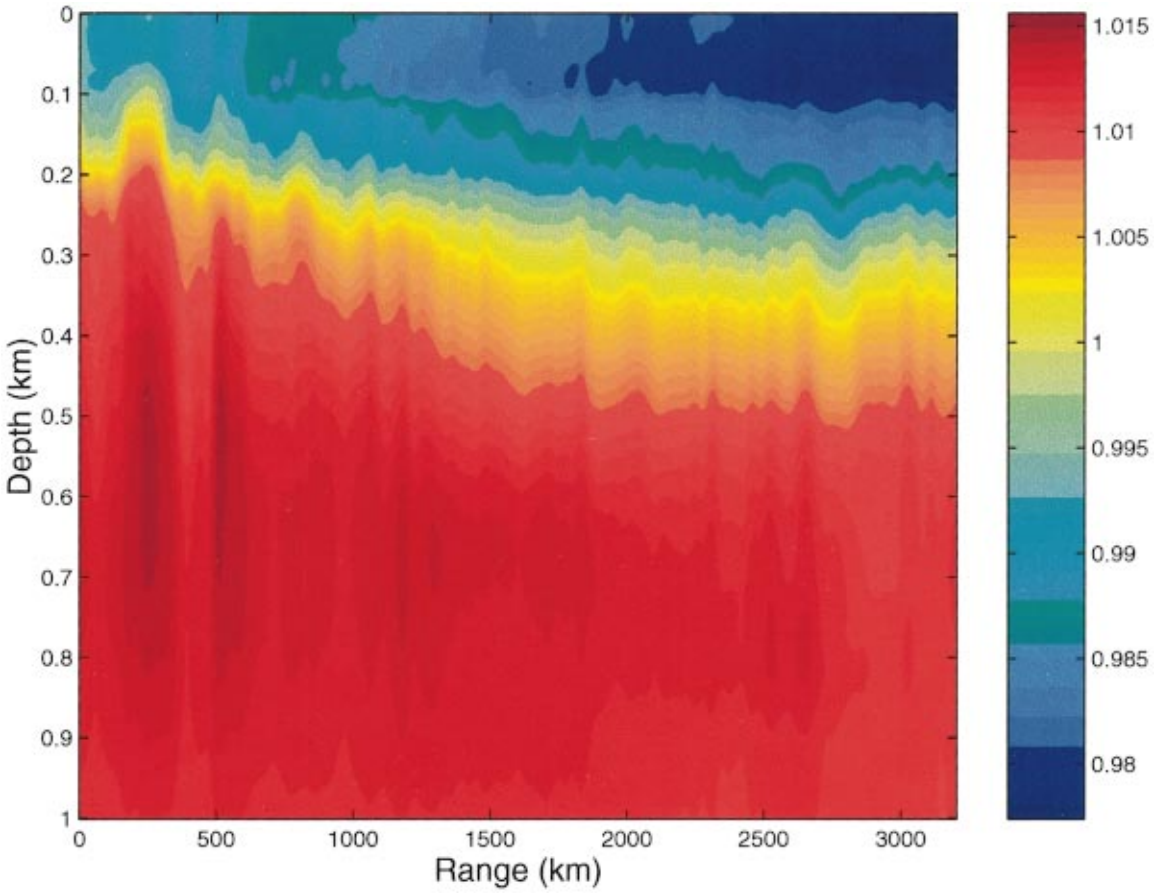

FIG. 19. (Color) The refractive index in the upper part of the waveguide at a range interval of 3000 km.

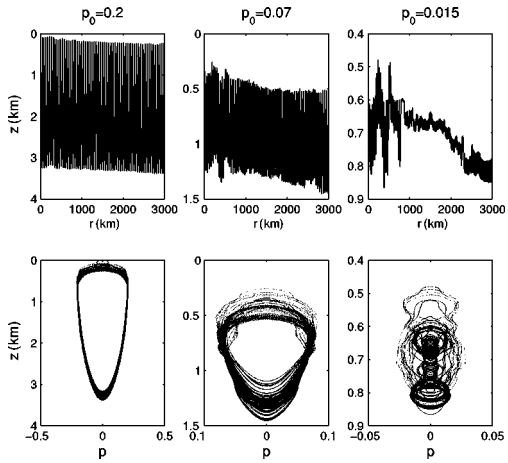

FIG. 20. Trajectories of three rays in the configuration (upper row of plots) and phase (lower row of plots) spaces. The rays start from the point set at 750 m depth with starting momenta $p_0=0.2$ (left column), $p_0=0.07$ (central column), and $p_0=0.015$ (right column).

Furthermore, irregular ''jumps'' of trajectories between different channels lead to chaotic behavior of near-axial rays.

So, the properties of mesoscale inhomogeneities differ from that of environmental models studied in Secs. II and III. Results of ray tracing presented below show how this difference reveals itself in ray dynamics.

B. Chaotic and regular rays

In our numerical simulations we have studied ray trajectories leaving a point source set at 750 m depth and propagating in the range-dependent environment presented in Figs. 18 and 19. The qualitative difference in behavior of near-axial and steeper ray paths is shown in Fig. 20. Here the trajectories of three rays are shown in configuration (upper row of plots) and phase (lower row) spaces. The steep ray with the starting momentum $p_0=0.2$ (left column) reveals a weak sensitivity to range variations of the sound-speed profile. The most part of its trajectory lies at large depths where the sound speed does not vary with range. A less steep trajectory with $p_0=0.07$ (middle column) is more sensitive to range variations in the environment. It gradually shifts to larger depths following the variation of the sound-channel axis seen in Fig. 18. However, this trajectory is still not affected significantly by mesoscale inhomogeneities. In contrast, the behavior of the near-axial ray with $p_0=0.015$ (right column) is almost completely determined by the mesoscale inhomogeneities: at every range the ray is trapped in one of local channels existing in this range, the ray ''jumps'' from one channel to another highly irregularly.

It is natural to expect that the coexistence of chaotic and regular rays should manifest itself in the time-front structure as it was the case for the idealized periodic environmental models considered in Secs. II and III.

The time front evaluated at 3000 km range is plotted in Fig. 21. It has been computed by tracing 20 000 fan rays with starting momenta uniformly incremented within the interval from -0.2 to 0.2. The early portion of the time front has the

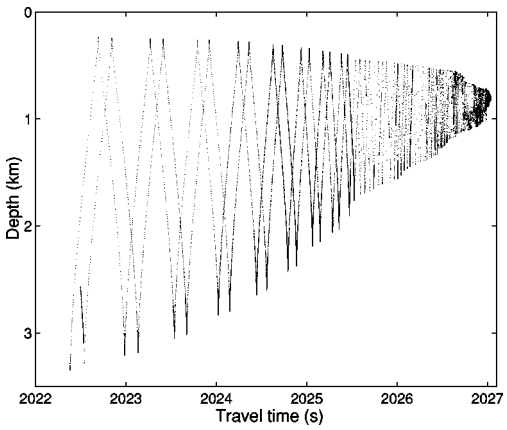

FIG. 21. The time front at 3000 km range.

folded accordion shape that we have already seen in Figs. 7 and 12. This shape is typical of unperturbed waveguides with smooth sound-speed profiles [8,12]. In the perturbed waveguides such shapes are observed in the portions of the time fronts formed by regular rays (see the lower panel in Fig. 7 and the middle row of plots in Fig. 12). As we go to large travel times the structure of the time front becomes irregular and this fact suggests that the late arrivals formed by near-axial rays are predominantly chaotic.

This expectation is consistent with the results presented in Fig. 22 where the travel time of the near-axial ray is shown versus the starting momentum. This plot is similar to those presented in Fig. 11 where the same dependencies are shown for chaotic rays in the waveguide with periodic inhomogeneity (30) superimposed on Munk profile (22). The lower panel in Fig. 22 presents the number of ray turning points as a function of p_0. We have already seen a similar dependence in Fig. 14. In both cases the extreme sensitivity to initial conditions is evident: a tiny variation of starting momentum often causes a significant change of trajectory shape. This result gives an evidence that the trajectories of near-axial rays propagating at small grazing angles are highly unstable. A

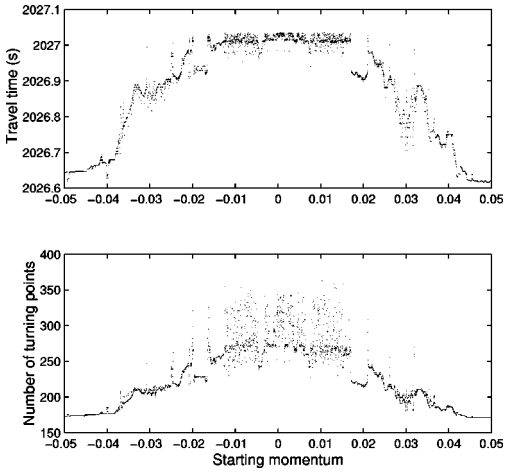

FIG. 22. Upper panel: Travel time dependence on the starting momentum for near-axial rays. Lower panel: Number of turning points as a function of starting momentum for near-axial rays.

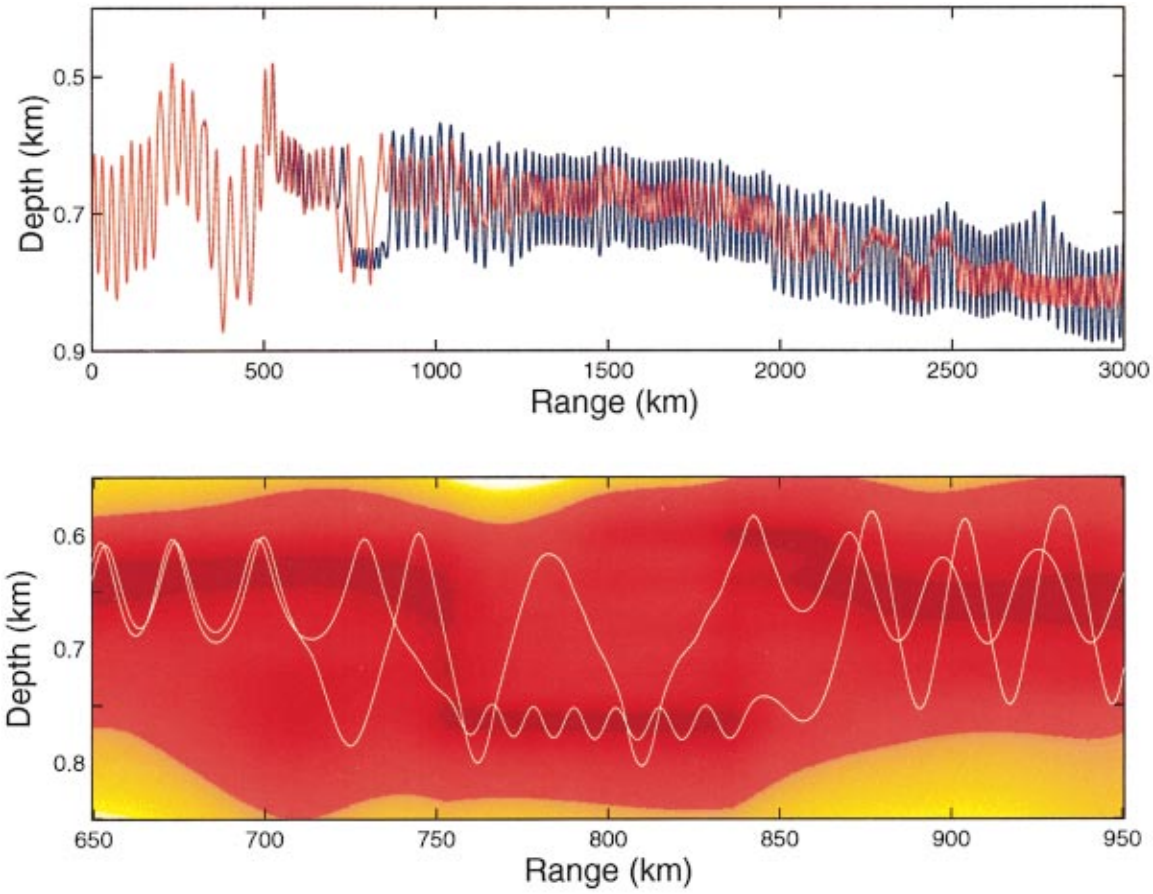

FIG. 23. (Color) Upper panel: Two ray trajectories starting from the point source at 750 m depth with initial momenta $p_0=0.015$ (red) and $p_0=0.01502$ (blue). Lower panel: A closer view of the trajectories in the range of 650–950 km. The spatial distribution of the ''potential'' U is shown by colors. The dark brown color corresponds to minima of $U(r,z)$, i.e., it indicates sound-channel axes of local waveguides formed by mesoscale inhomogeneities. The yellow color corresponds to large values of U, while intermediate values of U are marked by red.

detailed numerical analysis of ray paths has demonstrated that trajectories which are initially neighbors, move apart at an exponential rate. The Lyapunov exponents λ defined by Eq. (27) and representing the quantitative characteristic of this stochastic instability, varies from 1/100 1/km to 1/35 1/km.

The results of the ray tracing demonstrate that mesoscale inhomogeneities give rise to ray chaos similarly to what can appear due to the internal waves. However, the mechanisms of chaotic behavior are different for the two types of perturbations. This issue is a subject of the following section.

C. Mechanism of stochastic instability of near-axial rays and gaps in travel times

In the preceding sections we have discussed stochastic ray instability due to overlapping of different ray-medium resonances. This mechanism implies that a range-dependent perturbation ''responsible'' for emergence of ray chaos is weak [see conditions (19) and (20)]. For near-axial rays the fluctuations of the ''potential'' U in the vicinity of the sound-channel axis are of order of its mean value and the Hamiltonian (43) cannot be split into a sum of a smooth unperturbed term and a rapidly varying weak perturbation. In other words, near-axial rays cannot be treated in the scope of the perturbation theory described in Sec. II.

We suppose that the basic mechanism determining stochastic behavior of near-axial rays is related to the presence of irregular local waveguide channels in the depth interval of 500–800 m. This is illustrated in Fig. 23 where the trajectories of two rays with starting momenta $p_{01}=0.015$ (the same trajectory as in the upper right plot in Fig. 20) and $p_{02}=0.015\,02$ are shown. In the upper panel we see that both trajectories follow the same path up to 700 km range and then separate abruptly. The lower panel graphs these trajectories in the range of 650–950 km. The spatial distribution of the ''potential'' $U(r,z)$ are shown by colors. Dark colors correspond to small values of U, while light colors denote the larger values. Until 750 km range both trajectories propagate in the same local channel formed by mesoscale inhomogeneities, but beyond this range one of the trajectories is trapped into another channel located at larger depth (a fuzzy dark stripe at depths of about 750 m). Although at 850 km the ray returns back to its former channel, beginning from 750 km range the two trajectories follow different paths. Our numerical simulations show that this situation is typical and

''jumps'' of ray trajectories between neighboring local channels play an important role in emergence of stochastic instability. So, the mechanisms leading to chaotic dynamics of the near-axial and steep rays are different.

In spite of this difference, the numerical simulations demonstrate that the dynamics of near-axial rays have common features with the ray behavior observed in the preceding sections for steeper rays in idealized environmental models. The most typical and important of them is the coexistence of chaotic and regular rays. Starting momenta of rays can be divided into some intervals corresponding to the predominantly regular and predominantly chaotic rays.

In Sec. III it has been observed that the presence of a boundary between such intervals causes a gap in ray travel times. A similar phenomenon occurs for near-axial rays. The gaps are seen in the time front in Fig. 21 as the intervals of low density of points. The gaps are more apparent in the travel time dependence on the starting momentum, p_0, shown in the upper panel of Fig. 22. There are clusters of rays whose travel times differ considerably from that of neighboring rays. An example of such a cluster is represented by rays with p_0 close to 0.2. There is a gap of about 0.1 s between travel times of these rays and their neighbors. Looking at the lower panel of Fig. 22 we see that the gap in travel times corresponds to a gap in the number of ray turning points, i.e., rays with close times have similar ''topologies.''

VI. CONCLUSION

In this paper we have considered properties of chaotic ray dynamics in deep sea propagation models. The most part of the paper is devoted to studying of the waveguides with smooth range-independent sound-speed profiles perturbed by weak inhomogeneities with periodic range variations. Parameters of the perturbations have been chosen to model environmental variations induced by internal waves.

It has been demonstrated that the overlapping of nonlinear ray-medium resonances gives rise to ray chaos. Chirikov's criterion [14,16] has been applied to examine this mechanism of stochastic ray instability. A comparison of predictions made on the basis of Chirikov's criterion to numerical simulation results has shown that this approach allows one to make rough quantitative estimations characterizing sizes of regions in phase space occupied by chaotic rays. Furthermore, the phenomenon of resonance overlapping sheds some light on strong dependence of global ray sensitivity on the form of the unperturbed (background) sound-speed profile [8]. The key point here is that the background profile defines the interval of cycle lengths of the unperturbed rays, and the wider this interval is, more ray-medium resonances can exist for the given perturbation, and these resonances have more chances for overlapping and giving rise to strong ray chaos.

Another important issue addressed in this paper is chaotic properties of ray travel times. These characteristics of the wave field have received much attention in underwater acoustics because they are considered as main observables in schemes of acoustic monitoring of ocean structure [10,11]. We have examined extreme sensitivity of ray travel times to starting momenta and their fractal properties. In our numerical simulations it has been shown that in the presence of the perturbation giving rise to ray chaos, there appear gaps in the ray travel time distribution that are absent in the unperturbed waveguide. We argue that the presence of such gaps is related to coexistence of chaotic and nonchaotic rays. It has been shown that this phenomenon has a known analog in theory of dynamical chaos. It is the so-called stochastic particle acceleration [15]. A similar effect for chaotic rays that leads to appearance of gaps in the travel time distribution, we have called the stochastic ray acceleration.

Besides the variations in the environment induced by internal waves we have considered the influence of the so-called mesoscale inhomogeneities with significantly larger spatial scales. These inhomogeneities form local waveguides near the sound-channel axis and near-axial rays can be trapped in these channels and make irregular ''jumps'' from one channel to another.

It turns out that while the mesoscale inhomogeneities only slightly affect steep rays that remain regular, they give rise to chaos of near-axial rays propagating at small grazing angles. The most important feature of chaotic dynamics of near-axial rays is that it cannot be analyzed in the scope of perturbation theory based on smallness of perturbation. It requires the development of new approaches capable to describe how the ''jumps'' between different microchannels reveal themselves in ray travel times and other characteristics of the ray structure.

ACKNOWLEDGMENTS

We thank Dr. M. G. Brown for giving us sound-speed profiles constructed on the basis of the AET environmental measurements. This work was supported by the U.S. Navy Grant Nos. N00014-96-1-0055 and N00014-97-1-0426. The simulation was supported in part by the NSF cooperative agreement ACI-9619020 through computing resources provided by the National Partnership for Advanced Computational Infrastructure at the San Diego Supercomputer Center. A.V. and I.S. were partly supported by the Russian Foundation for Basic Research under Grant No. 00-02-17409.

[1] S. Abdullaev and G. Zaslavsky, Usp. Fiz. Nauk **161**(8), 1 (1991).

[2] S. Abdullaev, in *Chaos and Dynamics of Rays in Waveguide Media*, edited by G. Zaslovsky (Gordon and Breach, New York, 1993).

[3] D. Palmer, M. Brown, F. Tappert, and H. Bezdek, Geophys. Res. Lett. **15**, 569 (1988).

[4] M. Brown, F. Tappert, and G. Goni, Wave Motion **14**, 93 (1991).

[5] K. Smith, M. Brown, and F. Tappert, J. Acoust. Soc. Am. **91**,

1939 (1992).
[6] K. Smith, M. Brown, and F. Tappert, J. Acoust. Soc. Am. **91**, 1950 (1992).
[7] F. Tappert and X. Tang, J. Acoust. Soc. Am. **99**, 185 (1996).
[8] J. Simmen, S. Flatte, and G.-Y. Wan, J. Acoust. Soc. Am. **102**, 239 (1997).
[9] M. Wiercigroch, M. Badiey, J. Simmen, and A. H.-D. Cheng, J. Sound Vib. **220**, 771 (1999).
[10] W. Munk and C. Wunsch, Deep-Sea Res., Part A **26**, 123 (1979).
[11] J. Spiesberger and K. Metzger, J. Geophys. Res., [Oceans] **96**, 4869 (1991).
[12] P. F. Worcester *et al.*, J. Acoust. Soc. Am. **105**, 3185 (1999).
[13] J. A. Colosi *et al.*, J. Acoust. Soc. Am. **105**, 3202 (1999).
[14] B. Chirikov, Phys. Rep. **52**, 263 (1979).
[15] G. Zaslavsky and B. Chirkov, Usp. Fiz. Nauk **105**, 3 (1971) [Sov. Phys. Usp. **14**, 549 (1972)].
[16] A. Lichtenberg and M. Lieberman, *Regular and Chaotic Dynamics*, Applied Mathematical Sciences Vol. 38 (Springer Verlag, New York, 1992).
[17] S. Flatte, R. Dashen, W. Munk, K. Watson, and F. Zakhariasen, *Sound Transmission Through a Fluctuating Ocean* (Cambridge University Press, London, 1979).
[18] G. Zaslavsky and S. Abdullaev, Chaos **7**, 182 (1997).
[19] L. Landau and E. Lifshitz, *Mechanics* (Nauka, Moscow, 1973).
[20] F. Jensen, W. Kuperman, M. Porter, and H. Schmidt, *Computational Ocean Acoustics* (AIP, Woodbury, NY, 1994).
[21] T. Duda and J. Bowlin, J. Acoust. Soc. Am. **96**, 1033 (1994).
[22] L. Brekhovskikh and Y. Lysanov, *Fundamentals of Ocean Acoustics* (Springer-Verlag, Berlin, 1991).
[23] G. Zaslavsky, M. Edelman, and B. Niyazov, Chaos **7**, 159 (1997).
[24] E. Ott, *Chaos in Dynamical Systems* (Cambridge University Press, New York, 1993).
[25] G. Zaslavsky, *Physics of Chaos in Hamiltonian Systems* (Imperial College Press, Singapore, 1998).
[26] M. Wolfson and J. Spiesberger, J. Acoust. Soc. Am. **106**, 1293 (1999).
[27] S. Chin-Bing, D. King, and J. Boyd, *Oceanography and Acoustics: Prediction and Propagation Models*, edited by A. R. Robinson and D. Lee (AIP, New York, 1994), Chap. 1, pp. 7–49.